Atmospheric Environment 244 (2021) 117912

Contents lists available at ScienceDirect

Atmospheric Environment

journal homepage: http://www.elsevier.com/locate/atmosenv

Seasonal characteristics of aerosol vertical structure and autumn enhancement of non-spherical particle over the semi-arid region of northwest China

Tian Zhou [a], Hailing Xie [a], Tao Jiang [b], Jianping Huang [a,*], Jianrong Bi [a], Zhongwei Huang [a], Jinsen Shi [a]

[a] Key Laboratory for Semi-Arid Climate Change of the Ministry of Education, College of Atmospheric Sciences, Lanzhou University, Lanzhou, 730000, China
[b] College of Meteorology and Oceanography, National University of Defense Technology, Changsha, 410000, China

HIGHLIGHTS

- The spatiotemporal distribution of atmospheric aerosol behavior throughout a year were shown over SACOL region for the first time.
- The depolarization ratios (δ) in spring are higher than those in other seasons.
- Large differences of aerosol extinction coefficient (σ_a) in four seasons exist below 2 km, especially within 1 km.
- The enhancement of the coarse particles and smaller particles resulted in the sharp increase of σ_a and δ in autumn.

ARTICLE INFO

Keywords:
Seasonal characteristics
Aerosol vertical structure
Non-spherical particle enhancement
Lidar

ABSTRACT

Assessments of the effects of aerosols on the climate and environment still feature large uncertainties, and a better understanding of the spatiotemporal variation in these effects is needed. In this study, coincident observations of ground-based lidar and sun photometer measurements from March 2010 to February 2011 were selected to examine the sensible seasonal characteristics of the aerosol vertical structure and the potential variations of aerosol properties before and during the wintertime heating period at SACOL (Semi-Arid Climate and Environment Observatory of Lanzhou University, 35.946°N, 104.137°E, 1961 m ASL), northwest of China. Our results suggest that the aerosol behavior during a year can be roughly divided into two major periods: the non-spherical particle dominated period and the spherical particle dominated period based on the depolarization ratio, or the dust-dominated period (spring and winter) and the non-dust-dominated period (summer and autumn) based on the aerosol angstrom exponent. The height and width of peak of aerosol scale height frequency distribution show the distribution of aerosol layers in summer is highest, then followed by spring, autumn and winter. The depolarization ratios at different heights in spring are higher than those in other seasons. A similar distribution of extinction coefficients above 2 km can be seen in four seasons, but relatively large differences exist below 2 km, especially within 1 km. The increase of the extinction coefficient is observed near surface in November 2010 with a sharp increase in depolarization ratio which is induced by the rising contribution of the dust events (up to 13%) and the mixed type aerosols (70%). These results not only provide detailed characteristics of aerosol variation over the SACOL region, but also remind us to take into account the potential contribution of dust aerosol to the severe regional air pollution during the wintertime heating period.

1. Introduction

The radiative impact of atmospheric aerosol particles is one of the largest sources of uncertainty in accurately assessing their climate effects (IPCC, 2013). Atmospheric aerosol particles modulate the radiation budget of Earth's-climate system both directly and indirectly. They directly scatter and absorb incoming solar radiation and outgoing terrestrial radiation (Charlson et al., 1992; Huang et al., 2010a), and

* Corresponding author.
E-mail address: hjp@lzu.edu.cn (J. Huang).

https://doi.org/10.1016/j.atmosenv.2020.117912
Received 5 March 2020; Received in revised form 11 June 2020; Accepted 2 September 2020
Available online 3 September 2020

indirectly alter cloud properties by acting as cloud condensation nuclei or ice nuclei (Huang et al., 2015; Rosenfeld, 2000; Twomey, 1974). The quantification of aerosol climate effects is quite challenging due to their complex sources, large spatial and temporal variations, and complex mechanisms of their interaction with radiation and clouds (Ramanathan et al., 2001).

At present, research on aerosol optical, microphysical and chemical properties is relatively abundant, but studies on the vertical characteristics of aerosol is still scarce (Che et al., 2009). The uncertainty in the aerosol vertical structure alone can contribute as much as 0.5 W m^{-2} to the uncertainty in global aerosol forcing (Choi and Chung, 2014). Some previous studies have shown that when using column-integrated aerosol optical depth, column-mean single scattering albedo and asymmetry factor in calculations of the direct radiative forcing of aerosols, the vertical distribution of the aerosol extinction coefficient had very little impact at the top-of-the-atmosphere and surface but significantly changed the vertical profiles of the heating rate (Gadhavi and Jayaraman, 2006; Guan et al., 2010; Huang et al., 2009; Johnson et al., 2008), changed the stability of the atmosphere, and affected convection, turbulence and clouds (Lee, 2012; Li et al., 2018; Sun et al., 2019). The same aerosol type can produce different climatic effects (warming or cooling) and local feedbacks (snow/ice albedo and clouds) depending on its vertical location (Flanner, 2013). And also, the larger errors of the quantification of aerosol radiative effects can be introduced by the multi-layers aerosol transport or the elevated aerosol layer comprised different aerosol types (Das et al., 2013; Pani et al., 2016; Vuolo et al., 2014; Wang et al., 2010). Thus, it is of great significance to evaluate aerosol vertical structure and study the radiation and climate effects of aerosols.

The vertical structure of aerosols not only largely determines their residence and transport times (Bourgeois et al., 2015; Huang et al., 2008a) but also reflects the degree of aerosol loading (Sheng et al., 2019; Zhang et al., 2015; Zhou et al., 2013). Lidar, a powerful active remote sensing technique, has been widely used to detect the vertical distribution and spatiotemporal evolution of aerosols. Liu et al. (2012) and Fan et al. (2019) analyzed the seasonal characteristics of aerosol vertical structure at a site in the Yangtze River Delta region of China based on lidar measurements during 2008–2009 and 2013–2015, respectively. As reported by their studies, some elevated aerosol layers were traced back to northern/northwestern China, as far as Mongolia and Siberia, in spring, autumn and winter. Lee et al. (2019) analyzed the three-dimensional air quality structure using ground observation data and lidar measurements to identify vertical aerosol intrusion, and predicted haze pollution episodes caused by transboundary-transported heavy pollutants. The relationship between seasonal variations in aerosol optical depth and planetary boundary layer height was discussed by He et al. (2008). They pointed out that the contribution of aerosols within the planetary boundary layer to the monthly mean aerosol optical depth (AOD) is approximately 64% in Hong Kong. The similar studies were also reported by Kudo et al. (2018) using ground based measurements, and by Matthias et al. (2014) with chemistry transport models. Moreover, the aerosol vertical structure also affects the relationship between the AOD and the particle mass concentration (Chew et al., 2016; Zhao et al., 2018). Comparing different vertical distribution estimation approaches, Su et al. (2017) pointed out that the converted PM2.5 concentration from lidar-derived boundary layer heights shows the best agreement between retrievals and observations, with a correlation coefficient of 0.73.

Although the continuous measurements of the single ground-based lidar are not available for large regions, the climatology pattern of aerosol structure over the distinct environment can be determined. The vertical distributions of aerosol concentrations and properties in Dunhuang have already been focused by Iwasaka et al.(2003; 2004), and they strongly suggested that the non-spherical dust particles with large depolarization ratios frequently diffused in the free atmosphere. Using the aircraft measurements over the Loess Plateau, the vertical distributions of aerosol optical properties (including aerosol scattering coefficients, absorption coefficients and so on) were obtained, and the most of aerosol particles in the lower level originated from local or regional pollution emissions was indicated by Li et al. (2015). Based on the long-term measurements from SACOL and the short-term intensity observation field campaigns, many previous studies focused on the optical and microphysical properties of aerosols (Bi et al., 2016b, 2017; Liu et al., 2011; Zhang et al., 2019). Only several studies have been done on long-range transported dust cases and the vertical structure of atmospheric particles over SACOL region (Cao et al., 2013; Huang et al., 2010b; Wang et al., 2012; Xie et al., 2017; Zhang and Li, 2012; Zhou et al., 2018). Furthermore, the average profiles of aerosol extinction coefficient were only presented by these studies. There is no the detailed seasonal characteristics of the aerosol vertical structure over this region. In addition, the effects of human activities on aerosol properties cannot be ignored completely when the seasonal characteristics of aerosol properties are involved. Unlike the four seasons, the human activities are not so rigidly compartmentalized. For example, the beginning and duration of wintertime heating period vary among the different regions in northern China. Usually, the heating period starts in late autumn (even earlier), and then the anthropogenic pollution level rises due to the heating (Sheng et al., 2019). It is also found that the intensity and frequency of anthropogenic pollution in autumn are not less than those in spring and winter (Chen et al., 2014). Previous studies pointed out that the SACOL region is dominated by dust particles in spring, anthropogenic aerosols in summer and mixtures of dust with anthropogenic pollution in winter (Tian et al., 2018; Wang et al., 2013), but there are few clear conclusions about aerosols in autumn, and particularly nothing is known about the potential variations in aerosol properties associated with heating in November.

Therefore, this work aims to examine the sensible seasonal characteristics of aerosol vertical structure and then study the variation in aerosol vertical properties before and during the wintertime heating period based on the ground-based measurements at SACOL. The remainder of the paper is structured as follows: The instruments and data evolution are described in Section 2. The results and discussion are found in Section 3. A summary follows in Section 4.

2. Instrumentations and data processing

2.1. Site

SACOL, which is a permanent and rural station located on top of a mountain, is approximately 23 km in the straight-line distance from Lanzhou City. Some measurements (e.g. boundary layer meteorological, surface radiation, surface fluxes, soil parameters, ambient air, aerosol optical properties and vertical profiles, temperature and water vapor profiles) have been carried out at this site since 2006. In the past decade, the influence of urban expansion on atmospheric measurements has gradually emerged, especially aerosol measurements. These long-term and coincident measurements of multiple instruments were continuously conducted and provided many opportunities to study the process and properties of atmospheric aerosols over the semi-arid region, northwest China. More descriptions about station can be found in a previous study (Huang et al., 2008b).

2.2. Dual-wavelength polarization lidar

In this study, all vertical profiles of atmospheric aerosols were derived from the dual-wavelength polarization lidar which is the AD-Net standard system. The automated measurement of the lidar system was performed continuously at SACOL since October 2009. The lidar employs two-wavelength (532 and 1064 nm) Mie-scattering and polarization measurements at 532 nm. A telescope with a diameter of 20 cm is used to collect the backscattered light. Other specifications on hardware system can also be found in previous studies (Shimizu, 2004; Sugimoto

et al., 2002). Here, the most continuous lidar measurements from January 2010 to March 2011, and the measurements in October and November of 2009, 2011 and 2012 were selected to support our work.

Referring to the standard data processing of AD-Net, the overlap function of the laser and the field of view of the telescope were determined by observed profiles under well-mixed boundary layer conditions, and compensates the backscattering signal below 600 m (Shimizu, 2004). In this study, we defined the linear volume depolarization ratio, δ as:

$$\delta = P_{\perp}/P_{\parallel} \quad (1)$$

where $P_{\perp}$ and $P_{\parallel}$ are the backscattering signal intensity of perpendicular and parallel components, respectively. In order to eliminate the different sensitivity of the both polarization channels, a linear polarizer whose polarizing direction is inclined 45° to that of the cubic polarizer was placed in front of the cubic polarizer to obtain profiles for the calibration. As reported by some previous studies, the depolarization ratio of air pollution is very small (~0.05 ± 0.04), while that of pure dust (or fresh dust) is basically larger than 0.3 (Freudenthaler et al., 2009; Müller et al., 2014; Tesche et al., 2019). The similar summaries were also reported with the measurements of the dual-wavelength polarization lidar in AD-Net. As recommended by Shimizu et al. (2004), although 0.1 is large for a single spherical particle, the depolarization ratio of the region is less than 0.1 it is identified as spherical aerosol (anthropogenic pollution) which means an air mass contains spherical particles dominantly. Otherwise, the depolarization ratio of the region is greater than 0.1 it is identified as non-spherical aerosols. The depolarization ratio is larger than 0.3 for dust and is between 0.1 and 0.3 for mixed type aerosol (polluted dust or dust mixed with air pollution) (Sugimoto et al., 2015a).

The threshold method recommended by Sugimoto et al. (2015b) was used to remove clouds and heavy rain before applying an inversion method to the 15-min average lidar profiles. For our lidar system, the empirical threshold of upward gradient of the attenuated backscattering coefficient (ABC) is 1×10^{-8} $m^{-2}sr^{-1}$ for cloud base height. If the maximum of the ABC between cloud base and cloud top was less than 1×10^{-6} $m^{-1}sr^{-1}$, the feature layer was not identified as cloud. The rain was marked by the gradient threshold (beyond -5×10^{-17}) of signal below 2 km. Considering the annual variation of aerosol components, the AOD constrained Fernald method described by Huang et al. (2010b) was used to retrieve aerosol lidar ratios based on the coincident measurements of lidar and sun photometer. The brief steps are as follows: (1) selected the coincided measurement of lidar and sun photometer; (2) assumed the initial lidar ratio to retrieve the aerosol backscatter coefficient in the first iteration; (3) the $AOD_{AEROENT}$ (it could be represented by the column integrated aerosol extinction coefficient) at 532 nm was divided by column integrated aerosol backscatter coefficient to obtain the new lidar ratio; (4) compared the new lidar ratio with the previous lidar ratio, if the difference is greater than 5%, then the new lidar ratio was assigned to the next iteration again, and repeated steps (2) ~ (4); (5) the median value of lidar ratios in each month is as the monthly constant lidar ratio. Where, the boundary condition of the backward inversion method was set at 6 km. Rayleigh scattering from atmospheric molecules was calculated via the atmospheric density profile in the U.S. Standard Atmosphere (1976). The constant extinction coefficient within blind zone (200 m) was assumed, and it is equal to the value of the first height bin above blind zone. Then, the median value in each month represents the monthly constant lidar ratio which could be found in Table 1 of Supplementary. The aerosol backscatter coefficient β_a was further obtained using the backward inversion method (Fernald, 1984) with the assumption of monthly constant lidar ratio at 532 nm. The aerosol extinction coefficient σ_a was approximated from the β_a multiplied by the monthly constant lidar ratio. The σ_a is easily related to the column-integrated aerosol optical depth by:

Table 1
The percentage of anthropogenic pollution, mixed type and dust in October and November of 2010 and 2012. The three aerosol types were only identified with the thresholds of lidar depolarization ratios mentioned in section 2.2.

	2010		2012	
	Oct	Nov	Oct	Nov
Anthropogenic pollution	85	17	78	23
Mixed type	15	70	22	70
Dust	0	13	0	7

$$AOD_{\_lidar} = \int \sigma_a(z) \cdot dz \quad (2)$$

As shown by Fig. 1, the $AOD_{\_lidar}$ was compared with coincident $AOD_{\_AERONET}$ at 532 nm during range from Oct 2009 to Mar 2011. Where, the $AOD_{\_AERONET}$ at 532 nm was interpolated by the AODs at 440 nm and 675 nm (same hereinafter). The correlation coefficient of both independent AODs is about 0.8. The good consistency examines the extinction coefficient inversion with monthly constant lidar ratio, and could support the subsequent results.

2.3. Sun photometer

The CE-318 Sun photometer is the standard instrument of AERONET, and makes sun-tracking and sky scanning measurements every 15 min at wavelengths of 340, 380, 440, 500, 675, 870, 940 and 1020 nm (Holben et al., 1998). It can provide atmospheric columnar spectral-resolved AOD and aerosol inversion products (e.g., angstrom exponent and single scattering albedo; more products can be found on the AERONET homepage: http://aeronet.gsfc.nasa.gov). The AERONET products at SACOL are available from July 2006 to May 2013. In this study, only quality-assured datasets of version 3 level 2.0 corresponding to the lidar data were used. Notably, the AOD at 532 nm was calculated via interpolation of that at 440 nm and 675 nm.

3. Results and discussion

3.1. Measurement overview

To our knowledge, there is no related report presenting the time-height section of atmospheric aerosols at fixed station throughout the

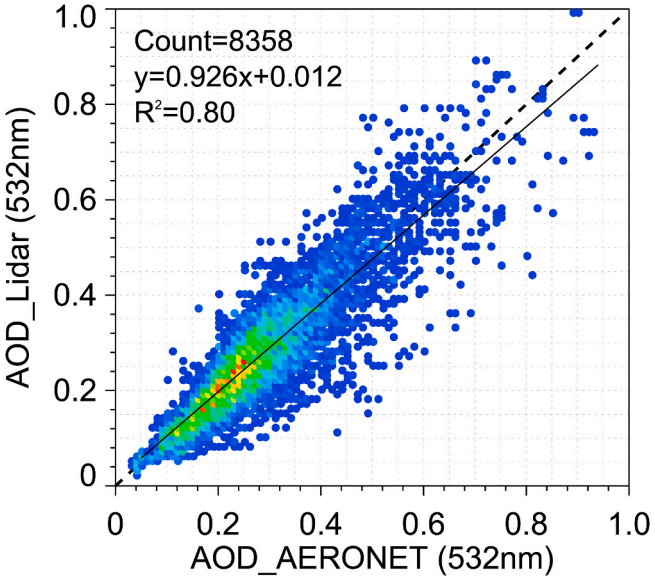

Fig. 1. The scatter plot of $AOD_{\_lidar}$ and $AOD_{\_AERONE}$ at 532 nm.

year over northwest China. Here, the overall time-height sections of atmospheric aerosol were given by the daily averaged aerosol extinction coefficient and daily averaged linear volume depolarization ratio. The temporal window from March 1, 2010 to February 28, 2011 was selected to exhibit the annual variation in aerosol behavior. As shown in Fig. 2(a) and (b), the aerosol layer distributions could be directly captured from the daily averaged extinction coefficient and depolarization ratio profiles. The significant indication confirmed by the linear volume depolarization ratio in Fig. 2(b) is that the aerosol behavior during a year can be roughly divided into two major periods: the non-spherical particle dominated period (late autumn, winter and spring) with high depolarization ratio, and the spherical particle dominated period (summer and early autumn, if several dust events during this period are ignored) with low depolarization ratio.

The AERONET daily averaged AOD at 532 nm and lidar-retrieved daily averaged AOD at 532 nm are also shown in Fig. 2(c). The $AOD_{\_AERONET}$ varies between 0.06 and 1.78, and the median value is 0.29 throughout the year. The AODs in spring are highest, and followed by winter. As pointed out by Dubovik et al. (2002), the value of angstrom exponent at 440–870 ($AE_{\_440\text{-}870}$) nm for dust aerosols with range from −0.1 to 0.6. The similar range between 0.3 and 0.7 was also reported by Smirnov et al. (2002), but for sea salt with low AOD at 440 nm. In the study by Bi et al. (2016a), they divided dust aerosol into two subtypes based on AERONET data over Central and East Asian (including SACOL station): the long-range transport polluted dust ($0.2 \leq AE_{\_440\text{-}870} \leq 0.6$) and the pure dust ($AE_{\_440\text{-}870} < 0.2$). Similar to the depolarization ratio$AE_{_440\text{-}870}$ threshold of 0.6 is used. Another intuitive distribution is also roughly divided into two major periods: the dust dominated period (spring and winter) and the non-dust dominated period (summer and autumn). According to the angstrom exponent thresholds recommended by Westphal et al. (1991) and Eck et al. (1999), the values of angstrom exponent ≤ 1 indicates size distributions dominated by coarse mode aerosols (radius ≥ 0.5 μm), and the values ≥ 0.2 indicate size distribution dominated by fine mode aerosols (radius ≤ 0.5 μm). Obviously, the most of circumstances in summer and autumn have the intermediate distributions.

Here, we were also attracted to the considerable oscillation of the $AE_{\_440\text{-}870}$ with a range of 0.2–1.3 from November to December 2010. During this period, the depolarization ratios in Fig. 2(b) sharply increase and remain high level. And also, this period coincides with the wintertime heating over the SACOL region. Therefore, this also encouraged us to analyze some variations in aerosol properties before and during the wintertime heating.

3.2. Aerosol vertical characteristics

3.2.1. Seasonal variation in vertical structure

The averaged profiles of the aerosol extinction coefficient and depolarization ratio in each season are shown in Fig. 3(a)–(d). Similar vertical patterns, in which values exponentially decrease with increasing height, can be found in the three seasons other than summer. The parts of the profiles below 2 km height in summer are nearly constant and are lower than 0.1 for both of the extinction coefficient and depolarization ratio. Over SACOL region, the measurements are frequently influenced by elevate-transported dust layers in free troposphere and dust events within the atmospheric boundary layer in spring. So, the depolarization ratios at different height in spring are higher than those in other seasons. While, the largest extinction coefficients exist near ground surface in winter due to the static weather and low visibility during this period.

Further, the modified aerosol scale heights (H_m) are derived from vertical profiles of aerosol extinction coefficient such that approximately 63% of the total $AOD_{\_lidar}$ exist below the height bin (Hayasaka et al., 2007). H_m is defined as

$$\int_0^{H_m} \sigma_a(z)\cdot dz = AOD_{\_lidar}(1-e^{-1}) \cong 0.6321\cdot AOD_{\_lidar} \quad (3)$$

The frequency functions of H_m with a 500 m interval are shown in

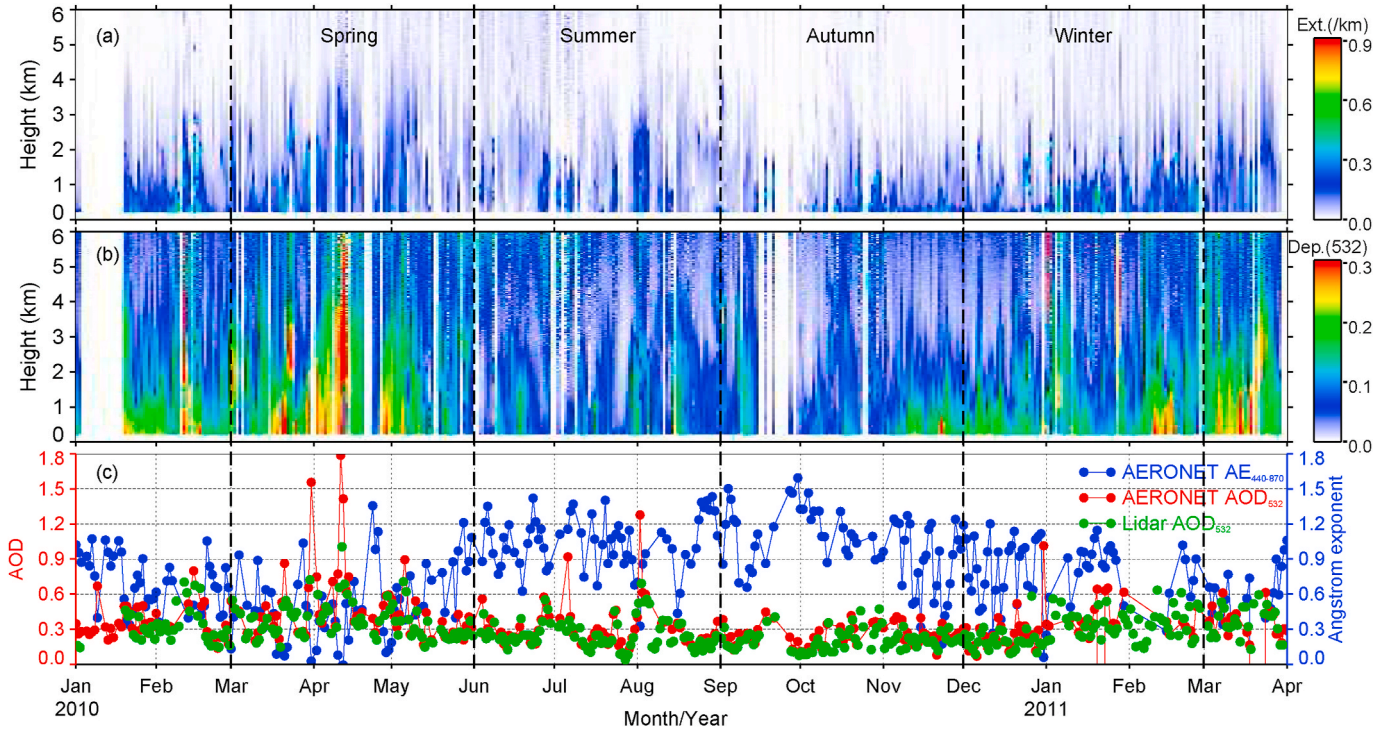

Fig. 2. The time series of the NIES lidar and sun photometer from January 1, 2010 to March 31, 2011. The time-height sections of (a) aerosol extinction coefficient and (b) linear volume depolarization ratio by NIES lidar. (c) aerosol optical depth at 532 nm (red dots) and angstrom exponent at 440–870 nm ($AE_{\_440\text{-}870}$, blue dots) from AERONET, aerosol optical depth (green dots) at 532 nm by NIES lidar. Each season is marked by black dashed lines. (For interpretation of the references to colour in this figure legend, the reader is referred to the Web version of this article.)

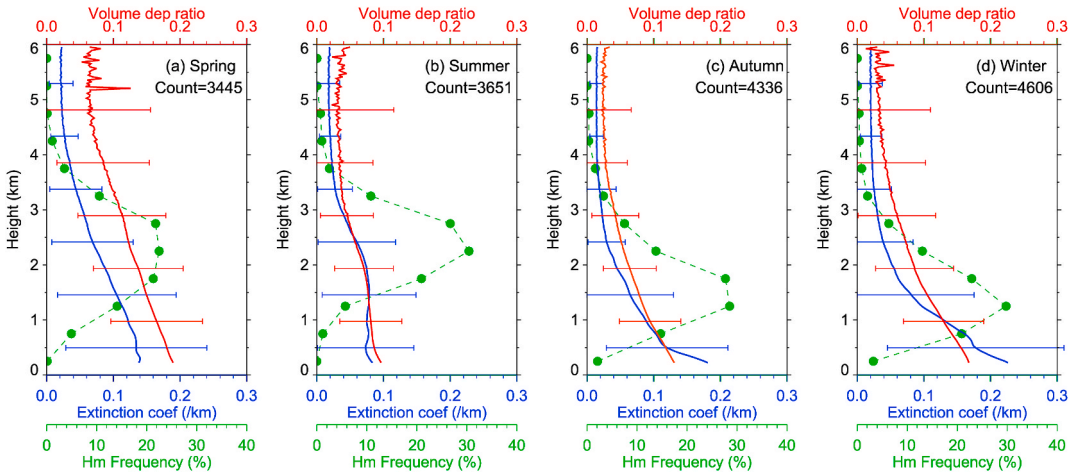

Fig. 3. The averaged profiles of the extinction coefficient (blue) and the linear volume depolarization ratio (red) with the standard deviation for (**a**) spring, (**b**) summer, (**c**) autumn and (**d**) winter. The frequency of the modified aerosol scale height (H_m) with 0.5 km interval was marked by green dots. (For interpretation of the references to colour in this figure legend, the reader is referred to the Web version of this article.)

Fig. 3. Overall, the most of H_m are bellow 4 km, and there is an unimodal distribution exists in each season. Considering the height and width of peak of H_m frequency distribution, it is shown that the distribution of aerosol layers is highest in summer, then followed by spring and autumn, and winter.

3.2.2. *Height-resolved vertical structure*

Here, the layer-averaged extinction coefficient and layer-averaged depolarization ratio were calculated within H_m. The normalized scatter plots of both are shown in Fig. 4(a)–(d). Excluding the summer, the large depolarization ratios are basically associated with the high extinction coefficients. The positive correlation between depolarization ratios and extinction coefficients implies the dust aerosols dominate

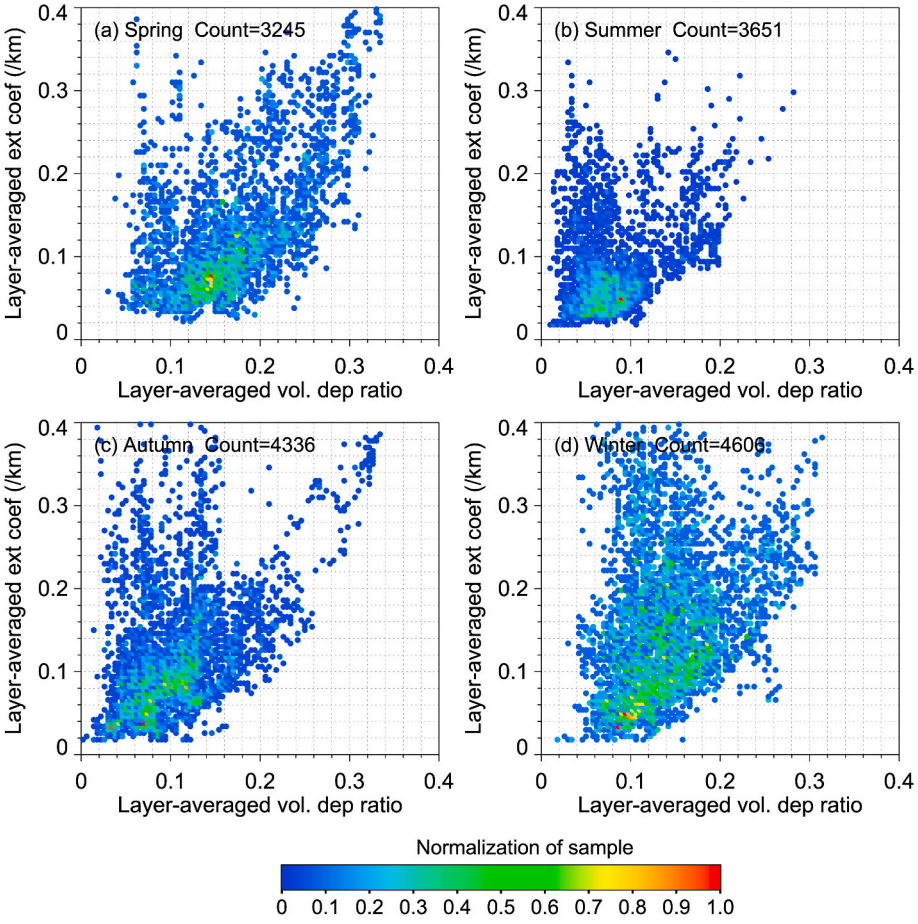

Fig. 4. Scatter plots between the layer-averaged volume depolarization ratio and layer-averaged extinction coefficient within H_m for (a) spring, (b) summer, (c) autumn and (d) winter.

atmospheric aerosol loading in spring. The similar positive correlation also exists in autumn and winter, but weaker. The rest of high extinction coefficients are dominated by the aerosol whose depolarization ratios are range of 0.02–0.16 and 0.08–0.2 in autumn and winter, respectively. To obtain more detailed vertical characteristics of aerosols in each season, the atmosphere from the ground to 6 km was divided into five layers in height. The lowest layer ranges from 0.2 km to 1 km. The extinction coefficients and depolarization ratios below H_m are analyzed in different height level. In summer, the convective boundary layer with approximately 3–4 km in height is often measured over SACOL region. Therefore, the highest layer between 4 km and 6 km was used to reflect the potential contribution of some long-range transported aerosol layers. As shown in Fig. 5(a)–(d), the histograms of the extinction coefficient and depolarization ratio also present some differences. Unimodal and similarly distributed extinction coefficients above 2 km are clearly present in all seasons. The relatively large differences exist below 2 km, especially within 1 km. In winter, the widest range of extinction coefficients reveals the sharp variation in aerosol loading near ground surface, and followed by spring and autumn. For the depolarization ratio, all layers cover a wide range in spring, and the maximum values are beyond 0.21. Similar conditions can also be seen in winter, but the peaks of the depolarization ratio in different level are lower. In addition, the depolarization ratios show the bimodal distribution below 4 km in autumn and 3–4 km in winter.

3.3. Variation in aerosol properties before and during wintertime heating

The winter season and heating period are not strictly coincident over the SACOL region. We collected the notices and news about winter heating in the past ten years from internet. The heating periods nearly all start on 1st November, and end on next 31 March in urban core. The heating in suburban and rural areas may be a few days earlier. In addition, according to our historical lidar measurements, a few dust events have been captured in November. Combining the results in autumn described above, we analyzed the aerosol properties in October and November to demonstrate the potential variation before and during the wintertime heating period. Then, the potential causes of sharp variations in the extinction coefficient, linear volume depolarization ratio and angstrom exponent were discussed.

3.3.1. Variation in vertical structure

Here, the historical lidar measurements during the first four years were selected to present the monthly profiles of the extinction coefficient and depolarization ratio in Fig. 6(a)–(d). Unfortunately, only a few profiles which were obtained from less than 10 days are available in 2009 and 2011. As shown by Fig. 6(a) and (c), these profiles do not represent the real situation very well. Therefore, the aerosol scale heights were only identified in 2010 and 2012. In Fig. 6(b) and (d), the similar trend is shown that both the extinction coefficients and depolarization ratios in the lower atmosphere increase in November via comparing that in October. The increase signifies the aerosol loading and the proportion of non-spherical particles significantly increase after wintertime heating beginning. Moreover, the frequency functions of aerosol scale height also suggest that the aerosol particles concentrate in lower height in November of these two years.

The height-resolved patterns in the vertical direction in 2010 and 2012 are similar to the profiles in Fig. 6. In Fig. 7(a) and (b), the aerosol extinction coefficients below 1 km exhibit a wider range after the heating beginning, and the depolarization ratios below 2 km increase obviously from October to November in both years. The differences between 2 and 4 km in 2010 are less significant than that in 2012. The values in the range of 4–6 km are resulted by the high aerosol scale heights which are induced by the two scenes in vertical. One is the clear sky with very low aerosol loading near ground surface during cold front passing. The other one is the coupling of the elevated aerosol layers and the aerosol layers with low loading near ground surface. Thus, it is clear that aerosol loading and non-spherical particles mainly increase near ground surface during the wintertime heating period.

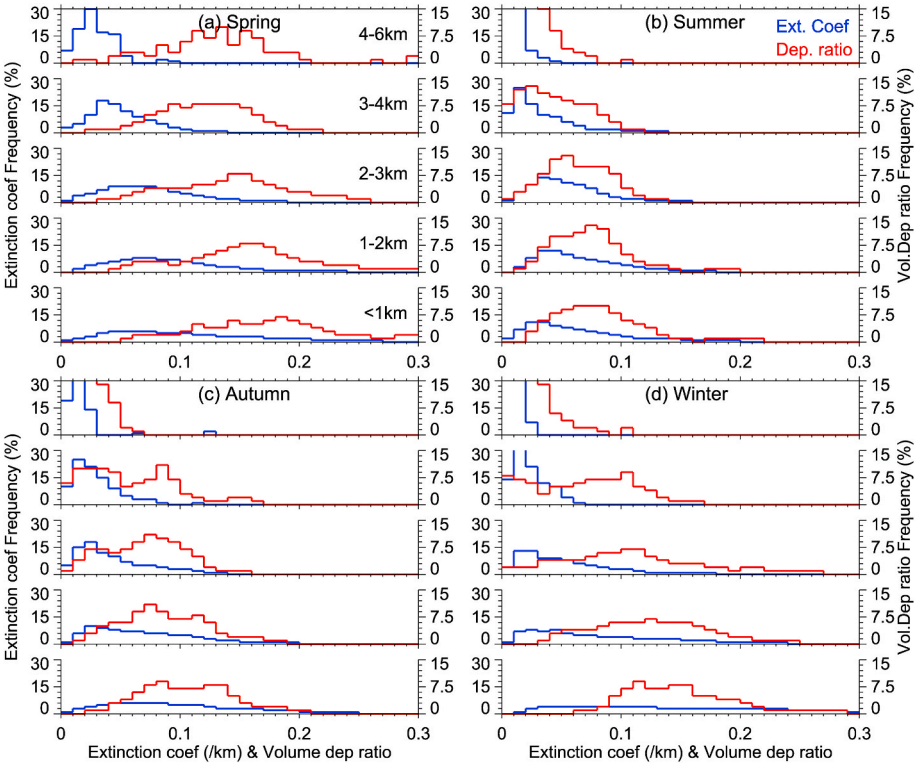

Fig. 5. Histograms of the frequency of the linear volume depolarization ratio (red) and extinction coefficient (blue) within H_m for (**a**) spring, (**b**) summer, (**c**) autumn and (**d**) winter. (For interpretation of the references to colour in this figure legend, the reader is referred to the Web version of this article.)

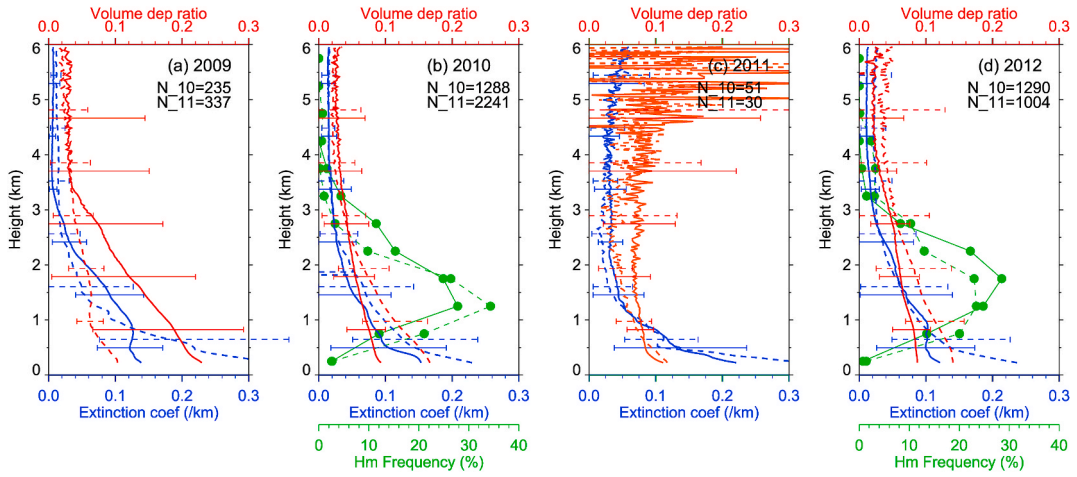

Fig. 6. Same as Fig. 3, but for October (Solid line) and November (dashed line) of (a) 2009, (b) 2010, (c) 2011 and (d) 2012.

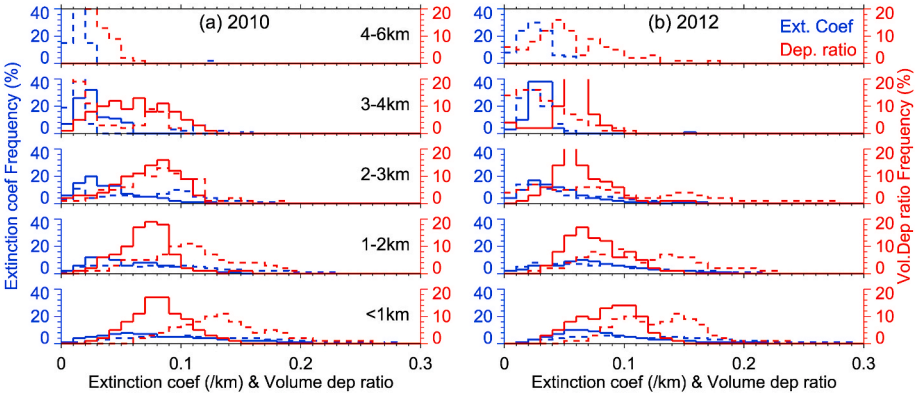

Fig. 7. Same as Fig. 4 but for (**a**) 2010 and (**b**) 2012. Solid and dashed lines denote October and November, respectively.

3.3.2. *Potential causes of* σ_a *and* δ *enhancement in November*

Coinciding with the lidar measurements, sun photometer measurements were used to further explore the differences in aerosol properties before and during the wintertime heating period. Several AERONET products, namely, AOD, particle size distribution and asymmetry factor, were considered only in October and November of 2009, 2010 and 2011. The measurement in 2012 is absent. There are sufficient samples with 11 days per month for these parameters, but only 8 days in October 2011. The limited data of single scattering albedo prevented us from trying to assess the variation in absorption properties.

Unlike the decrease of AOD in 2009 and the increase in 2010, there is almost no change of AOD at four wavelengths in October and November of 2011. To some extent, these trends of AOD are closely related to the variation of aerosol particle size distribution in both months. The fine mode and coarse mode are almost equivalent in both months of 2011 and in October of 2010. In 2009, the coarse mode dominates in both months, but it slightly weak in November. The most significant variation could be found in 2010. There, the coarse mode dominates in November, and the peak of the fine mode goes down from 0.25 μm to 0.11 μm. Comparing the mean $AE_{440\text{-}870}$ in 2009 and 2011, the decreasing amplitude of 0.22 also implies that the higher contribution of coarse particles in November of 2010. The asymmetry factor describes the angular distribution of the scattered radiation and determines whether the particles scatter radiation preferentially to the front or back. In Fig. 8 (g)–(i), the pattern of variation in November 2010, which decreases, flattens and slightly increases with wavelength, is different from the others. The increase at 870–1020 nm is possibly attributed to the higher contribution of large particles associated with dust, which is predominantly forward scattering. A similar trend was reported in the Yangtze River Delta and Beijing in China (Yu et al., 2011). Therefore, the significant increase of extinction coefficients near ground surface is attributed to the increase of the coarse particles and the smaller particles in November of 2010. The dust particles as coarse particle should be responsible for the sharply increase of depolarization ratios in this month. The similar situation may be guessed in 2012.

As for the increase of dust particles, we further analyzed the variations of three aerosol types (anthropogenic pollution, mixed type and dust mentioned in section 2.2) in both months of 2010 and 2012. As shown in Table 1, the percentages of the anthropogenic pollution in October of both years are higher than 78%. In November, the contribution of dust is 7%–13%, and that of mixed type aerosol increase up to about 70%. The similar scenarios also occur in December and January (as shown by the Figure- S3 in supplementary). These high percentages of mixed type aerosol are basically consistent with our practical measurements. That is: when the haze events outbreak during wintertime heating period, the depolarization ratios near ground surface show the intermediate values, so that it is difficult to distinguish dust from haze.

4. Summary and conclusions

In this study, the continuous ground-based lidar and coincident sun photometer measurements from March 2010 to February 2011 were selected to present the sensible seasonal characteristics of the aerosols vertical structure and the variation in aerosol properties associated with wintertime heating over the SACOL region, northwest China. Our results suggest that the aerosol behavior through a year over this region can be

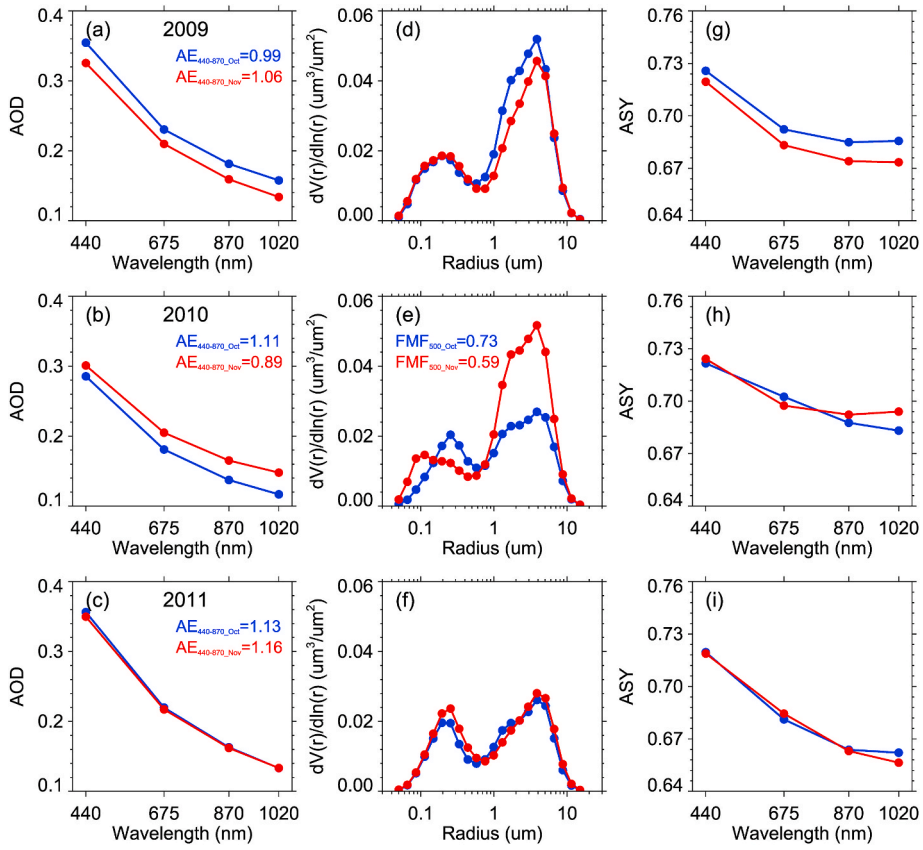

Fig. 8. The aerosol properties derived from AERONET products in (a, d, g) 2009, (b, e, h) 2010 and (c, f, i) 2011. (a–c) aerosol optical depth, (d–f) particle size distribution, (g–i) asymmetry factor. The blue and red dots denote October and November, respectively. (For interpretation of the references to colour in this figure legend, the reader is referred to the Web version of this article.)

roughly divided into two major periods: the non-spherical particle dominated period and the spherical particle dominated period based on the depolarization ratio, or the dust dominated period (spring and winter) and the non-dust dominated period (summer and autumn) based on the aerosol angstrom exponent. Considering the height and width of peak of aerosol scale height frequency distribution, the distribution of aerosol layers in summer is highest, then followed by spring, autumn and winter. The depolarization ratios at different heights in spring are higher than those in other seasons. For the extinction coefficient, a similar distribution above 2 km is evident in all seasons, but relatively large differences exist below 2 km, especially within 1 km. Through analyzing the one monthly-averaged aerosol properties before and during the wintertime heating period, the increase of the extinction coefficient is observed near surface in November 2010 with a sharp increase in depolarization ratio which is induced by the rising contribution of the dust events (up to 13%) and the mixed type aerosols (70%). The similar situation may be guessed in 2012.

Here, the limited sun photometer measurements in 2009, 2011 and 2012 prevent us from understanding the optical and microphysical properties of aerosol before and during the wintertime heating period. However, the potential similarities have been identified in the increases in the aerosol extinction coefficient and depolarization ratio during the heating period in 2012. Meanwhile, the uncertainties were also revealed by the differences of the optical and microphysical properties of aerosols during this period. For example, is the effect of human heating activities (e.g biomass burning, fossil fuel) on aerosol properties consistent during the early stage of each heating period? What extent is the potential effect of different degree of dust aerosol loading on anthropogenic pollution properties during wintertime heating period? These results encourage us to continuously focus on these issues through the combination of available measurements and simulation data.

CRediT authorship contribution statement

These authors contributed equally: Tian Zhou, Hailing Xie **Tian Zhou:** Conceptualization, Data curation, Funding acquisition, Investigation, Methodology, Writing - original draft. **Hailing Xie:** Conceptualization, Data curation, Investigation, Methodology, Validation, Visualization. **Tao Jiang:** Investigation, Validation, Visualization. **Jianping Huang:** Conceptualization, Investigation, Methodology. **Jianrong Bi:** Data curation, Investigation. **Zhongwei Huang:** Data curation, Investigation. **Jinsen Shi:** Data curation, Investigation.

Declaration of competing interest

The authors declare that they have no known competing financial interests or personal relationships that could have appeared to influence the work reported in this paper.

Acknowledgments

This work was supported by the National Science Foundation of China (No. 41975019, 41627807), the Second Tibetan Plateau Scientific Expedition and Research Program (STEP) (2019QZKK0602), Innovative Research Groups of the National Science Foundation of China (grant no. 41521004) and the Fundamental Research Funds for the Central University (lzujbky-2019-42). Sun photometer data were obtained through the AERONET website (http://aeronet.gsfc.nasa.gov/cgi-bin/webtool_opera_v2_inv). We also acknowledge all anonymous reviewers for their insightful and valuable comments.

Appendix A. Supplementary data

Supplementary data to this article can be found online at https://doi.org/10.1016/j.atmosenv.2020.117912.

References

Bi, J., Huang, J., Holben, B., Zhang, G., 2016a. Comparison of key absorption and optical properties between pure and transported anthropogenic dust over East and Central Asia. Atmos. Chem. Phys. 16, 15501–15516.

Bi, J., Huang, J., Holben, B., Zhang, G., 2016b. Comparison of key absorption and optical properties between pure and transported anthropogenic dust over East and Central Asia. Atmos. Chem. Phys. 16, 15501–15516.

Bi, J., Huang, J., Shi, J., Hu, Z., Zhou, T., Zhang, G., Huang, Z., Wang, X., Jin, H., 2017. Measurement of scattering and absorption properties of dust aerosol in a Gobi farmland region of northwestern China - a potential anthropogenic influence. Atmos. Chem. Phys. 17, 7775–7792.

Bourgeois, Q., Ekman, A.M.L., Krejci, R., 2015. Aerosol transport over the andes from the amazon basin to the remote pacific ocean: a multiyear CALIOP assessment. J. Geophys. Res.: Atmosphere 120, 8411–8425.

Cao, X., Wang, Z., Tian, P., Wang, J., Zhang, L., Quan, X., 2013. Statistics of aerosol extinction coefficient profiles and optical depth using lidar measurement over Lanzhou, China since 2005-2008. J. Quant. Spectrosc. Radiat. Transfer 122, 150–154.

Charlson, R.J., Schwartz, S.E., Hales, J.M., Cess, R.D., Coakley, J.A., Hansen, J.E., Hofmann, D.J., 1992. Climate forcing BY anthropogenic aerosols. Science 255, 423–430.

Che, H., Yang, Z., Zhang, X., Zhu, C., Ma, Q., Zhou, H., Wang, P., 2009. Study on the aerosol optical properties and their relationship with aerosol chemical compositions over three regional background stations in China. Atmos. Environ. 43, 1093–1099.

Chen, Z., Wenqing, L., Jianguo, L., Tianshu, Z., Yunsheng, D., B, G., F, M., M, A., 2014. Using lidar, in-situ measurements and trajectory analysis to observe air pollution in Beijing. EPJ Web Conf. 119, 24008.

Chew, B.N., Campbell, J.R., Hyer, E.J., Salinas, S.V., Reid, J.S., Welton, E.J., Holben, B. N., Liew, S.C., 2016. Relationship between aerosol optical depth and particulate matter over Singapore: effects of aerosol vertical distributions. Aerosol Air Qual. Res. 16, 2818–2830.

Choi, J.-O., Chung, C.E., 2014. Sensitivity of aerosol direct radiative forcing to aerosol vertical profile. Tellus B 66, 24376.

Das, S., Chen, J.-P., Madineni, V.R., Achuthan, J., 2013. Investigation of radiative effects of the optically thick dust layer over the Indian tropical region. Ann. Geophys. 31, 647–663.

Dubovik, O., Holben, B., Eck, T.F., Smirnov, A., Kaufman, Y.J., King, M.D., Tanre, D., Slutsker, I., 2002. Variability of absorption and optical properties of key aerosol types observed in worldwide locations. J. Atmos. Sci. 59, 590–608.

Eck, T.F., Holben, B.N., Reid, J.S., Dubovik, O., Smirnov, A., O'Neill, N.T., Slutsker, I., Kinne, S., 1999. Wavelength dependence of the optical depth of biomass burning, urban, and desert dust aerosols. J. Geophys. Res. Atmos. 104, 31333–31349.

Fan, W., Qin, K., Xu, J., Yuan, L., Li, D., Jin, Z., Zhang, K., 2019. Aerosol vertical distribution and sources estimation at a site of the Yangtze River Delta region of China. Atmos. Res. 217, 128–136.

Fernald, F.G., 1984. Analysis of atmospheric lidar observations - some comments. Appl. Optic. 23, 652–653.

Flanner, M.G., 2013. Arctic climate sensitivity to local black carbon. J. Geophys. Res. Atmos. 118, 1840–1851.

Freudenthaler, V., Esselborn, M., Wiegner, M., Heese, B., Tesche, M., Ansmann, A., Mueller, D., Althausen, D., Wirth, M., Fix, A., Ehret, G., Knippertz, P., Toledano, C., Gasteiger, J., Garhammer, M., Seefeldner, A., 2009. Depolarization ratio profiling at several wavelengths in pure Saharan dust during SAMUM 2006. Tellus Ser. B Chem. Phys. Meteorol. 61, 165–179.

Gadhavi, H., Jayaraman, A., 2006. Airborne lidar study of the vertical distribution of aerosols over Hyderabad, an urban site in central India, and its implication for radiative forcing calculations. Ann. Geophys. 24, 2461–2470.

Guan, H., Schmid, B., Bucholtz, A., Bergstrom, R., 2010. Sensitivity of shortwave radiative flux density, forcing, and heating rate to the aerosol vertical profile. J. Geophys. Res. Atmos. 115.

Hayasaka, T., Satake, S., Shimizu, A., Sugimoto, N., Matsui, I., Aoki, K., Muraji, Y., 2007. Vertical distribution and optical properties of aerosols observed over Japan during the atmospheric brown clouds-east Asia regional experiment 2005. J. Geophys. Res. Atmos. 112.

He, Q., Li, C., Mao, J., Kai-Hon, A., Lau, A., Chu, D., 2008. Analysis of aerosol vertical distribution and variability in Hong Kong. J. Geophys. Res. 113.

Holben, B.N., Eck, T.F., Slutsker, I., Tanre, D., Buis, J.P., Setzer, A., Vermote, E., Reagan, J.A., Kaufman, Y.J., Nakajima, T., Lavenu, F., Jankowiak, I., Smirnov, A., 1998. Aeronet - a federated instrument network and data archive for aerosol characterization. Remote Sens. Environ. 66, 1–16.

Huang, J., Fu, Q., Su, J., Tang, Q., Minnis, P., Hu, Y., Yi, Y., Zhao, Q., 2009. Taklimakan dust aerosol radiative heating derived from CALIPSO observations using the Fu-Liou radiation model with CERES constraints. Atmos. Chem. Phys. 9, 4011–4021.

Huang, J., Minnis, P., Chen, B., Huang, Z., Liu, Z., Zhao, Q., Yi, Y., Ayers, J.K., 2008a. Long-range transport and vertical structure of Asian dust from CALIPSO and surface measurements during PACDEX. J. Geophys. Res.: Atmosphere 113.

Huang, J., Minnis, P., Yan, H., Yi, Y., Chen, B., Zhang, L., Ayers, J.K., 2010a. Dust aerosol effect on semi-arid climate over Northwest China detected from A-Train satellite measurements. Atmos. Chem. Phys. 10, 6863–6872.

Huang, J., Zhang, W., Zuo, J., Bi, J., Shi, J., Wang, X., Chang, Z., Huang, Z., Yang, S., Zhang, B., Wang, G., Feng, G., Yuan, J., Zhang, L., Zuo, H., Wang, S., Fu, C., Chou, J., 2008b. An overview of the semi-arid climate and environment research observatory over the Loess Plateau. Adv. Atmos. Sci. 25, 906–921.

Huang, J.P., Liu, J.J., Chen, B., Nasiri, S.L., 2015. Detection of anthropogenic dust using CALIPSO lidar measurements. Atmos. Chem. Phys. 15, 11653–11665.

Huang, Z., Huang, J., Bi, J., Wang, G., Wang, W., Fu, Q., Li, Z., Tsay, S.-C., Shi, J., 2010b. Dust aerosol vertical structure measurements using three MPL lidars during 2008 China-US joint dust field experiment. J. Geophys. Res. Atmos. 115.

IPCC, 2013. Climate Change: Work Group Contribution to the IPCC Fifth Assessment Report (AR5).

Iwasaka, Y., Shi, G.Y., Kim, Y.S., Matsuki, A., Trochkine, D., Zhang, D., Yamada, M., Nagatani, T., Nagatani, M., Shen, Z., Shibata, T., Nakata, H., 2004. Pool of dust particles over the Asian continent: balloon-borne optical particle counter and ground-based lidar measurements at Dunhuang, China. Environ. Monit. Assess. 92, 5–24.

Iwasaka, Y., Shibata, T., Nagatani, T., Shi, G.Y., Kim, Y.S., Matsuki, A., Trochkine, D., Zhang, D., Yamada, M., Nagatani, M., Nakata, H., Shen, Z., Li, G., Chen, B., Kawahira, K., 2003. Large depolarization ratio of free tropospheric aerosols over the Taklamakan Desert revealed by lidar measurements: possible diffusion and transport of dust particles. J. Geophys. Res. Atmos. 108.

Johnson, B.T., Heese, B., McFarlane, S.A., Chazette, P., Jones, A., Bellouin, N., 2008. Vertical distribution and radiative effects of mineral dust and biomass burning aerosol over West Africa during DABEX. J. Geophys. Res. Atmos. 113.

Kudo, R., Aoyagi, T., Nishizawa, T., 2018. Characteristics of aerosol vertical profiles in Tsukuba, Japan, and their impacts on the evolution of the atmospheric boundary layer. Atmos. Meas. Tech. 11, 3031–3046.

Lee, H.-J., Jo, H.-Y., Kim, S.-W., Park, M.-S., Kim, C.-H., 2019. Impacts of atmospheric vertical structures on transboundary aerosol transport from China to South Korea. Sci. Rep. 9.

Lee, S.S., 2012. Dependence of the effect of aerosols on cirrus clouds on background vertical velocity. Atmos. Res. 111, 79–89.

Li, J., Jian, B., Huang, J., Hu, Y., Zhao, C., Kawamoto, K., Liao, S., Wu, M., 2018. Long-term variation of cloud droplet number concentrations from space-based Lidar. Remote Sens. Environ. 213, 144–161.

Li, J., Liu, X., Yuan, L., Yin, Y., Li, Z., Li, P., Ren, G., Jin, L., Li, R., Dong, Z., Li, Y., Yang, J., 2015. Vertical distribution of aerosol optical properties based on aircraft measurements over the Loess Plateau in China. J. Environ. Sci. 34, 44–56.

Liu, J., Zheng, Y., Li, Z., Flynn, C., Cribb, M., 2012. Seasonal variations of aerosol optical properties, vertical distribution and associated radiative effects in the Yangtze Delta region of China. J. Geophys. Res.: Atmosphere 117.

Liu, Y., Huang, J., Shi, G., Takamura, T., Khatri, P., Bi, J., Shi, J., Wang, T., Wang, X., Zhang, B., 2011. Aerosol optical properties and radiative effect determined from sky-radiometer over Loess Plateau of Northwest China. Atmos. Chem. Phys. 11, 11455–11463.

Müller, D., Hostetler, C., Ferrare, R., Burton, S., Chemyakin, E., Kolgotin, A., Hair, J., Cook, A., Harper, D., Rogers, R., Hare, R., Cleckner, C., Obland, M., Tomlinson, J., Berg, L., Schmid, B., 2014. Airborne Multiwavelength High Spectral Resolution Lidar (HSRL-2) observations during TCAP 2012: vertical profiles of optical and microphysical properties of a smoke/urban haze plume over the northeastern coast of the US. Atmos. Meas. Tech. Discuss. 7.

Matthias, V., Aulinger, A., Bieser, J., Quante, M., 2014. The relation of the planetary boundary layer height to the vertical aerosol distribution in chemistry transport models. In: Steyn, D.G., Builtjes, P.J.H., Timmermans, R.M.A. (Eds.), Air Pollution Modeling and its Application Xxii, pp. 553–557.

Pani, S.K., Wang, S.-H., Lin, N.-H., Tsay, S.-C., Lolli, S., Chuang, M.-T., Lee, C.-T., Chantara, S., Yu, J.-Y., 2016. Assessment of aerosol optical property and radiative effect for the layer decoupling cases over the northern South China Sea during the 7-SEAS/Dongsha Experiment. J. Geophys. Res. Atmos. 121, 4894–4906.

Ramanathan, V., Crutzen, P.J., Lelieveld, J., Mitra, A.P., Althausen, D., Anderson, J., Andreae, M.O., Cantrell, W., Cass, G.R., Chung, C.E., Clarke, A.D., Coakley, J.A., Collins, W.D., Conant, W.C., Dulac, F., Heintzenberg, J., Heymsfield, A.J., Holben, B., Howell, S., Hudson, J., Jayaraman, A., Kiehl, J.T., Krishnamurti, T.N., Lubin, D., McFarquhar, G., Novakov, T., Ogren, J.A., Podgorny, I.A., Prather, K., Priestley, K., Prospero, J.M., Quinn, P.K., Rajeev, K., Rasch, P., Rupert, S., Sadourny, R., Satheesh, S.K., Shaw, G.E., Sheridan, P., Valero, F.P.J., 2001. Indian Ocean Experiment: an integrated analysis of the climate forcing and effects of the great Indo-Asian haze. J. Geophys. Res. Atmos. 106, 28371–28398.

Rosenfeld, D., 2000. Suppression of rain and snow by urban and industrial air pollution. Science 287, 1793–1796.

Sheng, Z., Che, H., Chen, Q., Xia, X.a., Liu, D., Wang, Z., Zhao, H., Gui, K., Zheng, Y., Sun, T., Li, X., Liu, C., Wang, H., Wang, Y., Zhang, X., 2019. Aerosol vertical distribution and optical properties of different pollution events in Beijing in autumn 2017. Atmos. Res. 215, 193–207.

Shimizu, A., 2004. Continuous observations of Asian dust and other aerosols by polarization lidars in China and Japan during ACE-Asia. J. Geophys. Res. 109.

Shimizu, A., Sugimoto, N., Matsui, I., Arao, K., Uno, I., Murayama, T., Kagawa, N., Aoki, K., Uchiyama, A., Yamazaki, A., 2004. Continuous observations of Asian dust and other aerosols by polarization lidars in China and Japan during ACE-Asia. J. Geophys. Res. Atmos. 109.

Smirnov, A., Holben, B.N., Kaufman, Y.J., Dubovik, O., Eck, T.F., Slutsker, I., Pietras, C., Halthore, R.N., 2002. Optical properties of atmospheric aerosol in maritime environments. J. Atmos. Sci. 59, 501–523.

Su, T., Li, J., Li, C., Lau, A.K.-H., Yang, D., Shen, C., 2017. An intercomparison of AOD-converted PM2.5 concentrations using different approaches for estimating aerosol vertical distribution. Atmos. Environ. 166, 531–542.
Sugimoto, N., Matsui, I., Shimizu, A., Uno, I., Asai, K., Endoh, T., Nakajima, T., 2002. Observation of dust and anthropogenic aerosol plumes in the Northwest Pacific with a two-wavelength polarization lidar on board the research vessel Mirai. Geophys. Res. Lett. 29, 7-1-7-4.
Sugimoto, N., Nishizawa, T., Shimizu, A., Matsui, I., Kobayashi, H., 2015a. Detection of internally mixed Asian dust with air pollution aerosols using a polarization optical particle counter and a polarization-sensitive two-wavelength lidar. J. Quant. Spectrosc. Radiat. Transfer 150, 107–113.
Sugimoto, N., Shimizu, A., Nishizawa, T., Matsui, I., Jin, Y., Khatri, P., Irie, H., Takamura, T., Aoki, K., Thana, B., 2015b. Aerosol characteristics in Phimai, Thailand determined by continuous observation with a polarization sensitive Mie-Raman lidar and a sky radiometer. Environ. Res. Lett. 10.
Sun, T., Che, H., Qi, B., Wang, Y., Dong, Y., Xia, X., Wang, H., Gui, K., Zheng, Y., Zhao, H., Ma, Q., Du, R., Zhang, X., 2019. Characterization of vertical distribution and radiative forcing of ambient aerosol over the Yangtze River Delta during 2013-2015. Sci. Total Environ. 650, 1846–1857.
Tesche, M., Kolgotin, A., Haarig, M., Burton, S.P., Ferrare, R.A., Hostetler, C.A., Müller, D., 2019. 3+2 + X: what is the most useful depolarization input for retrieving microphysical properties of non-spherical particles from lidar measurements using the spheroid model of Dubovik et al. (2006)? Atmos. Meas. Tech. 12, 4421–4437.
Tian, P., Zhang, L., Cao, X., Sun, N., Mo, X., Liang, J., Li, X., Gao, X., Zhang, B., Wang, H., 2018. Enhanced bottom-of-the-atmosphere cooling and atmosphere heating efficiency by mixed-type Aerosols: a classification based on aerosol nonsphericity. J. Atmos. Sci. 75, 113–124.
Twomey, S., 1974. Pollution and the planetary albedo. Atmos. Environ. 8, 1251–1256, 1967.
Vuolo, M.R., Schulz, M., Balkanski, Y., Takemura, T., 2014. A new method for evaluating the impact of vertical distribution on aerosol radiative forcing in general circulation models. Atmos. Chem. Phys. 14, 877–897.
Wang, H., Zhang, L., Cao, X., Zhang, Z., Liang, J., 2013. A-Train satellite measurements of dust aerosol distributions over northern China. J. Quant. Spectrosc. Radiat. Transf. 122, 170–179.
Wang, S.-H., Lin, N.-H., Chou, M.-D., Tsay, S.-C., Welton, E.J., Hsu, N.C., Giles, D.M., Liu, G.-R., Holben, B.N., 2010. Profiling transboundary aerosols over Taiwan and assessing their radiative effects. J. Geophys. Res. Atmos. 115.
Wang, Z., Zhang, L., Cao, X., Huang, J., Zhang, W., 2012. Analysis of dust aerosol by using dual-wavelength lidar. Aerosol Air Qual. Res. 12, 608–614.
Westphal, D.L., Toon, O.B., 1991. Simulations of microphysical, radiative, and dynamic processes in a continental-scale forest-fire smoke plume. J. Geophys. Res. Atmos. 96, 22379–22400.
Xie, H., Zhou, T., Fu, Q., Huang, J., Huang, Z., Bi, J., Shi, J., Zhang, B., Ge, J., 2017. Automated detection of cloud and aerosol features with SACOL micro-pulse lidar in northwest China. Optic Express 25, 30732–30753.
Yu, X., Zhu, B., Yin, Y., Fan, S., Chen, A., 2011. Seasonal variation of columnar aerosol optical properties in Yangtze River Delta in China. Adv. Atmos. Sci. 28, 1326–1335.
Zhang, J., Li, X., 2012. Vertical distribution of sand-dust aerosols and the relationships with atmospheric environment. J. Arid Land 4, 357–368.
Zhang, Y., Zhang, Q., Leng, C., Zhang, D., Cheng, T., Tao, J., Zhang, R., He, Q., 2015. Evolution of aerosol vertical distribution during particulate pollution events in Shanghai. J. Meteorol. Res. 29, 385–399.
Zhang, Z., Huang, J., Chen, B., Yi, Y., Liu, J., Bi, J., Zhou, T., Huang, Z., Chen, S., 2019. Three-year continuous observation of pure and polluted dust aerosols over northwest China using the ground-based lidar and sun photometer data. J. Geophys. Res. Atmos. 124, 1118–1131.
Zhao, H., Che, H., Wang, Y., Dong, Y., Ma, Y., Li, X., Hong, Y., Yang, H., Liu, Y., Wang, Y., Gui, K., Sun, T., Zheng, Y., Zhang, X., 2018. Aerosol vertical distribution and typical air pollution episodes over northeastern China during 2016 analyzed by ground-based lidar. Aerosol Air Qual. Res. 18, 918–937.
Zhou, T., Huang, J., Huang, Z., Liu, J., Wang, W., Lin, L., 2013. The depolarization–attenuated backscatter relationship for dust plumes. Optic Express 21, 15195–15204.
Zhou, T., Xie, H., Bi, J., Huang, Z., Huang, J., Shi, J., Zhang, B., Zhang, W., 2018. Lidar measurements of dust aerosols during three field campaigns in 2010, 2011 and 2012 over northwestern China. Atmosphere 9.